Available online at www.sciencedirect.com
SCIENCE DIRECT®
Journal of Solid State Chemistry 172 (2003) 396–411
JOURNAL OF SOLID STATE CHEMISTRY
http://elsevier.com/locate/jssc

Crystal structure, thermal expansion and conductivity of anisotropic $La_{1-x}Sr_xGa_{1-2x}Mg_{2x}O_{3-y}$ ($x = 0.05$, 0.1) single crystals

L. Vasylechko,[a,b,*] V. Vashook,[c] D. Savytskii,[a] A. Senyshyn,[a] R. Niewa,[b] M. Knapp,[d] H. Ullmann,[c] M. Berkowski,[e] A. Matkovskii,[a,f] and U. Bismayer[g]

[a] *Institute of Telecommunications, Radioelectronics and Electronics Technique, Lviv Polytechnic National University, 12 Bandera St., Lviv 79013, Ukraine*
[b] *Max-Planck-Institut für Chemische Physik fester Stoffe, Nöthnitzerstrasse 40, Dresden D-01187, Germany*
[c] *Institute of Physical Chemistry and Electrochemistry, Dresden University of Technology, Dresden D-01062, Germany*
[d] *Institute for Materials Science, Darmstadt University of Technology, Petersenstrasse 23, Darmstadt D-64287, Germany*
[e] *Institute of Physics Polish Academy of Sciences, Al. Lotników 32/46, Warsaw 02-668, Poland*
[f] *Institute of Physics, HPU, 16 Rejtana St., Rzeszow 35-310, Poland*
[g] *University of Hamburg, Grindelallee 48, Hamburg D-20146, Germany*

Received 30 July 2002; received in revised form 22 November 2002; accepted 24 November 2002

Abstract

Crystal structure and anisotropy of the thermal expansion of single crystals of $La_{1-x}Sr_xGa_{1-2x}Mg_{2x}O_{3-y}$ ($x = 0.05$ and 0.1) were measured in the temperature range 300–1270 K. High-resolution X-ray powder diffraction data obtained by synchrotron experiments have been used to determine the crystal structure and thermal expansion. The room temperature structure of the crystal with $x = 0.05$ was found to be orthorhombic (*Imma*, $Z = 4$, $a = 7.79423(3)$ Å, $b = 5.49896(2)$ Å, $c = 5.53806(2)$ Å), whereas the symmetry of the $x = 0.1$ crystal is monoclinic (*I*2/*a*, $Z = 4$, $a = 7.82129(5)$ Å, $b = 5.54361(3)$ Å, $c = 5.51654(4)$ Å, $\beta = 90.040(1)^\circ$). The conductivity in two orthogonal directions of the crystals has been studied. Both, the conductivity and the structural data indicate three phase transitions in $La_{0.95}Sr_{0.05}Ga_{0.9}Mg_{0.1}O_{2.92}$ at 520–570 K (*Imma*–*I*2/*a*), 770 K (*I*2/*a*–*R*3*c*) and at 870 K (*R*3*c*–*R*-3*c*), respectively. Two transitions at 770 K (*I*2/*a*–*R*3*c*) and in the range 870–970 K (*R*3*c*–*R*-3*c*) occur in $La_{0.9}Sr_{0.1}Ga_{0.8}Mg_{0.2}O_{2.85}$.

Keywords: Sr- and Mg-doped $LaGaO_3$; Single crystals; Perovskites; Crystal structure; Thermal expansion; Phase transitions; Conductivity

1. Introduction

Several publications described different aspects of transport and structure properties of Sr- and Mg-doped lanthanum gallates (LSGM) [1–7]. These materials are of interest as potential electrolytes in solid oxide fuel cells. Nevertheless, there are uncertainties concerning the crystal structure. Feng and Goodenough [2] reported a cubic structure for $La_{0.9}Sr_{0.1}Ga_{0.8}Mg_{0.2}O_{2.85}$ (LSGM-10) at room temperature (RT), whereas Ishihara et al. [3] described the crystal structure of pure and doped $LaGaO_3$ to be orthorhombic (OR). Drennan et al. [4] by X-ray diffraction, scanning and transmission electron microscopy observed an OR (space group *Pnma*) structure for LSGM-10 at RT and a phase transition to rhombohedral (Rh) structure at 445 K. Based on high-resolution powder neutron diffraction data, Slater et al. [5,6] concluded that the RT structure is monoclinic (Mcl) (space group *I*2/*a*). Two-phase transitions appear between 723 and 1273 K: monoclinic(pseudo-OR)–monoclinic(pseudo-Rh)–rhombohedral (*R*3*c*). Recently, Lerch et al. [7] investigated the structure of $La_{0.9}Sr_{0.1}Ga_{0.8}Mg_{0.2}O_{2.85}$ using powder neutron diffraction at 273, 1073, and 1273 K. The authors reported a distorted perovskite-type structure (space group *Imma*) for the RT phase and an ideal cubic perovskite-type structure (*Pm*3*m*) for the HT-modification.

The discrepancies described above are not surprising because LSGM adopts a perovskite-type structure with extremely weak deformations from the cubic aristotype. It is very difficult to distinguish between different kinds

*Corresponding author. Fax: +38-0322-742164.
E-mail address: crystal@polynet.lviv.ua (L. Vasylechko).

0022-4596/03/$ - see front matter © 2003 Elsevier Science (USA). All rights reserved.
doi:10.1016/S0022-4596(03)00016-1

of slightly distorted perovskite-type structures by convenient X-ray powder diffraction methods. The variants of the structure differ mainly in the amount of distortion arising from the coupled tilting of corner-shared BO_6 octahedra. Such deformations can be recognized in powder diffraction patterns from the splitting of the main perovskite diffraction intensities and/or by the appearance of weak superstructure reflections arising from the concomitant enlargement of the unit cell. High-resolution powder diffraction techniques with high signal-to-noise ratios are required to detect such small structural deformations.

Thermal expansions of Sr- and Mg-doped $LaGaO_3$ samples have been measured by some authors [2, 8–10]. Ishihara et al. [8] reported linear thermal expansion for $LaGaO_3$-based oxides with an average thermal expansion coefficient of $11.0\times10^{-6}\,K^{-1}$ from RT to 1570 K. This value is slightly larger than the value reported by Feng and Goodenough [2]. The replacement of La by Sr increases the thermal expansion slightly. Hayashi et al. [10] measured the thermal expansion of Sr- and Mg-doped $LaGaO_3$ in the temperature range 100–873 K using a push-rod differential dilatometer. The thermal expansion coefficients became larger with increasing Sr and Mg contents, leading to smaller binding energies in the oxides in the presence of oxygen vacancies. All measurements mentioned above were performed on polycrystalline ceramic samples and hence, only average thermal expansion coefficients were reported. No data on the thermal expansion of LSGM single crystals in different crystallographic directions are so far available in the literature.

Electrical conductivities of A- and B-site doped lanthanum gallates have been measured by several investigators [1–3, 11–13]. Experimental set-ups were used in order to increase the ionic conductivity, and to suppress the electronic conductivity, or to enhance mixed conduction of $LaGaO_3$. Highest conductivity values were found in $La_{0.9}Sr_{0.1}Ga_{0.8}Mg_{0.2}O_{3-x}$ [11]. The activation energy of the conductivity of LSGM ceramics varies from 1.08 to 0.74 eV depending on sample composition and temperature range. All conductivity measurements were carried out on ceramic samples. The investigation of single crystalline samples could detect anisotropies of physical properties in different crystallographic directions and correlations between structural features and ionic conductivity.

In the present study the high-resolution powder diffraction technique using synchrotron radiation has been applied to determine the structure of $La_{1-x}Sr_xGa_{1-2x}Mg_{2x}O_{3-y}$ ($x=0.05$ and 0.1) crystals and its precise evolution with temperature. Small peak half-widths and high collimation and signal-to-noise ratios allow to observe even slight deviations between lattice parameters and to detect very weak superstructure reflections.

2. Experimental

$La_{1-x}Sr_xGa_{1-2x}Mg_{2x}O_{3-y}$ ($x=0.05$ and 0.1) single crystals with diameters of 15 mm and lengths of 25–30 mm were grown from the melt in Ar atmosphere using the Czochralski technique. In order to determine the composition chemical analysis of the crystals has been carried out. The La content was determined from sulfuric acid solution by direct titration with Trilon B (Ga was masked by acetylacetone). The amount of Ga was determined by substitutional titration using Cu comlexonat and Trilon B (La was masked by NH_4F). For the Sr and Mg analysis, samples were melted using $Na_2CO_3+Na_4B_2O_7\times10H_2O$ flux. The melt was dissolved in HCl (1:1). The Mg concentration was determined by atomic absorption spectroscopy using an AAS-1N spectrometer (Carl Zeiss, Jena) with a propene/butane/air flame at wavelength 285.2 nm. Sr was determined by atomic-emission spectroscopy (Carl Zeiss, Jena) at wavelength 470.7 nm. Our chemical analysis gives evidence that the cation concentration in the crystals is practically identical to that of the starting compositions (Table 1).

Examination of the crystals at RT by a Guinier transmission camera (HUBER image plate, Cu$K\alpha_1$ radiation, $\lambda=1.54056$ Å) showed pure perovskite-type structure for both crystals. No traces of additional phases were detected. DTA/DSC examination of the LSGM-05 crystal using a STA 409 calorimeter (NETZSCH, Selb, SiC-furnace, heating rate 10.0 K/min) from RT to 970 K showed an endothermic signal on heating indicating a phase transformation at 718 K. The transition was found to be reversible and the corresponding exothermal peak has been observed on cooling at 698 K. Examination of the LSGM-10 crystal did not reveal any further phase transition up to 1670 K.

It is well-known that $RGaO_3$ crystals, and especially $LaGaO_3$, has a strong tendency of twin formation [14–16]. Reasons for twinning in $LaGaO_3$ are the structural phase transition at 420 K as well as weak deviations from a paraelastic cubic structure. In LSGM the deviation from the paraelastic cubic structure is even smaller than in $LaGaO_3$, and therefore, the twin structure of LSGM crystals is more complex. This twinning is further enhanced by structural instabilities.

Attempts to separate single domain specimens suitable for single-crystal measurements were not successful. The Laue pattern of a twinned LSGM-05 crystal is shown in Fig. 1. The splitting of the reflections results from the twin structure. Because of the strong twinning, the crystal structure had finally to be studied by the powder diffraction technique. For this purpose, the crystals were crushed, powdered in agate mortar, and powders were sieved through the 20 μm mesh. In order to study the LSGM structure and its thermal evolution in detail in the temperature range from 300 to 1260 K

Table 1
Chemical analysis of the LSGM-05 and LSGM-10 crystals

Sample	Contents	La_2O_3 (wt%)	SrO (wt%)	Ga_2O_3 (wt%)	MgO (wt %)	Composition
LSGM-05	Nominal	62.323	2.086	33.968	1.623	$La_{0.95}Sr_{0.05}Ga_{0.9}Mg_{0.1}O_{2.92}$
	Experimental	62.39	2.25	33.47	1.69	$La_{0.953}Sr_{0.054}Ga_{0.888}Mg_{0.105}O_{2.92}$
LSGM-10	Nominal	61.086	4.317	31.238	3.359	$La_{0.9}Sr_{0.1}Ga_{0.8}Mg_{0.2}O_{2.85}$
	Experimental	60.99	4.47	31.17	3.37	$La_{0.898}Sr_{0.103}Ga_{0.798}Mg_{0.201}O_{2.85}$

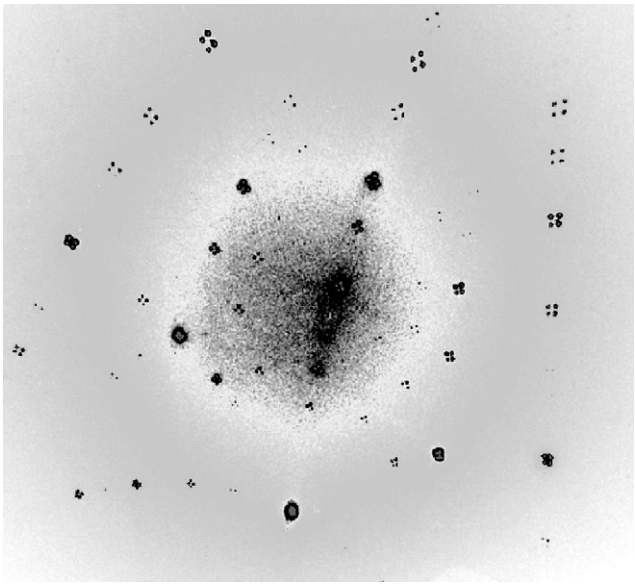

Fig. 1. Laue pattern for a LSGM-05 crystal, obtained using the microbeam (Lawrence Berkeley National Laboratory, Advanced Light Source). Reflections are split into four individual peaks due to twinning.

high-resolution powder diffraction experiments have been performed at the synchrotron laboratory HASYLAB [17]. The diffraction experiments were carried out using the powder diffractometer (beamline B2), equipped with a STOE furnace. For beam conditioning a Ge (111) double-crystal monochromator and a Ge (111) crystal analyzer in front of a NaI scintillation counter were inserted. The wavelength was calibrated using the positions of five silicon reflections. The sample was mounted inside a STOE furnace in Debye–Scherrer geometry equipped with a Eurotherm temperature controller and a capillary spinner.

In order to detect the critical temperatures and to obtain the thermal expansion coefficients measurements of the thermal evolution of 25 characteristic reflections were carried out in the temperature range 300–1260 K. To obtain precise reflection positions, intensities and values of HWFMs for every peaks, the experimental profiles were fitted using the profile decomposition program PROFAN [18]. Lattice parameters were refined by least-squares method taking into account the refinement of the "zero shift" values. Full diffraction patterns were collected at RT and 1260 K for the LSGM-10 sample and at RT, 670, 820 and 1020 K for LSGM-05. Structure refinement was performed by the full-profile Rietveld method using the program package WinCSD [18].

For conductivity measurements twinned single-crystal plates of 1 mm thickness with a surface area 20–50 mm^2 were cut from crystal boules with two orientations, perpendicular and parallel to the pulling axis, respectively. X-ray examination of the large surfaces of the plates cut perpendicular to the pulling axis showed the presence of $(001)_o$, $(211)_o$ and $(010)_o$ oriented domains with predominance of the $(211)_o$ ones. Surfaces oriented parallel to the pulling axis showed the presence of $(100)_o$ and $(011)_o$ blocks. The Miller's indices correspond to OR symmetry with *Imma* space group. The relative amount of domains with different orientations could be estimated for each sample from the intensity ratios of the corresponding reflections.

The plates were coated with platinum paste (Heraeus) sintered at 1270 K for 1 h in air. Platinum wires with 0.1 mm diameter were attached to the samples. A quasi-four-point method was used for AC conductivity measurements in air in the temperature range 300–1300 K with a heating/cooling rate of 3.5 K/min. The measurements were carried out using a HP4284 device computer controlled at four frequencies (100, 1000, 10,000, and 100,000 Hz). The imaginary part of the resistance was small in comparison with the real part, and the real part did not change significantly with frequency.

3. Results and discussion

Investigation of the samples using high-resolution powder diffraction techniques and synchrotron radiation at RT confirmed single-phase compositions of both LSGM-05 and LSGM-10 samples. No traces of other phases were detected, even by high-resolution technique with very high signal-to-noise ratio. Extremely narrow diffraction peaks of LSGM (typical HWFM values were 0.013–0.03°) similar to those of pure $LaGaO_3$ and $NdGaO_3$ single crystals indicate the homogeneity of the crystals.

Very high resolution of the diffraction patterns allows to observe reflection splitting, which could not be detected by classical X-ray techniques. The character of the splitting (number of reflections and their relative intensities) indicated the OR distortions of the perovskite-type structure. Analysis of systematic absences indicated a body-centered lattice. All reflections of the RT patterns were indexed according to the body-centered OR lattice. The refined values of the lattice parameters were as follows: $a = 7.7942$ Å, $b = 5.4990$ Å, $c = 5.5381$ Å for LSGM-05 and $a = 7.7.8211$ Å, $b = 5.5165$ Å, $c = 5.5435$ Å for LSGM-10. As shown in Section 3.2, the RT structures of both LSGM-10 and LSGM-05 in the temperature range 570–720 K are in fact Mcl.

3.1. Thermal expansion

The analysis of the thermal evolution of the experimental profiles showed the splitting of reflections typical of an OR distortion of the perovskite lattice. The splitting remains visible up to 670 and 720 K for the LSGM-05 and LSGM-10, respectively. Above these temperatures the character of splitting changes drastically. As an example, the thermal evolution of the $(020)_o + (211)_o + (002)_o$ triplet of the LSGM-10 sample is shown in Fig. 2. On heating from 770 K the magnitudes of the OR peaks decrease and disappear completely above 870 K. Simultaneously, additional reflections appear in the pattern. The reflection splitting above 870 K clearly indicates Rh symmetry for the HT phases. At 770 K co-existence of both OR and Rh phases has been found. As it was recently reported [19,20], the

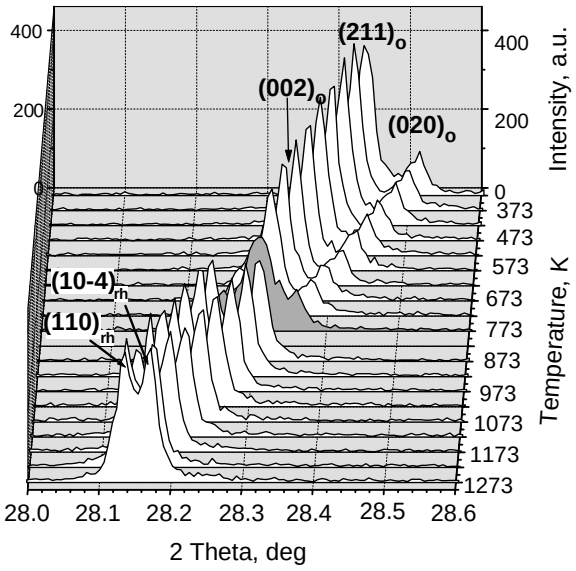

Fig. 2. Thermal evolution of $(211)_o + (002)_o + (020)_o$ triplet and $(10\text{-}4)_{rh} + (110)_{rh}$ doublet of the LSGM-10 structure in the temperature range 300–1260 K.

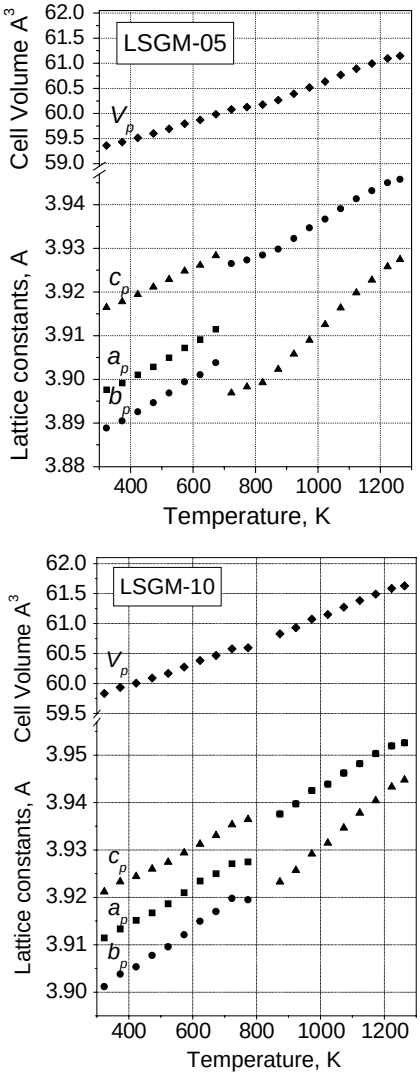

Fig. 3. Thermal expansion of the LSGM-05 and LSGM-10 crystals in the temperature range 300–1260 K. Lattice constants of OR and Rh phases normalized to the pseudo-cubic perovskite cell according to: $a_{pc} = a_o/2$, $b_{pc} = b_o/\sqrt{2}$, $c_{pc} = c_o/\sqrt{2}$, $a_{pc} = a_{rh}/\sqrt{2}$, $c_{pc} = c_{rh}/\sqrt{12}$.

simultaneous presence of RT and HT phases (in some temperature regions of the phase transformation) is typical for $La_{1-x}RE_xGaO_3$ solid solutions. Rh distortions remain visible at least up to 1260 K for both samples. The splitting of reflections indicating the deviation from the cubic lattice in LSGM-10 at HT is extremely small (typically, 0.02–0.04°). Only high collimation of the synchrotron beam allows it to detect.

The temperature dependences of the lattice parameters and cell volumes of the crystals are presented in Fig. 3. Due to the very weak distortion the lattice parameters of LSGM-05 below 673 K and LSGM-10 below 770 K are refined in OR symmetry. It is evident that a rhombohedral-to-monoclinic (pseudo-OR) phase transition in the LSGM-05 and LSGM-10 crystals occurs at temperatures 720 and 770 K, respectively.

Table 2
Linear thermal expansion coefficients (K^{-1}) of LSGM-05 and LSGM-10 along different crystallographic directions

	LSGM-05		LSGM-10	
	300–670 K (*Imma* and *I*2/*a* structures)	720–1260 K (*R*3*c* and *R*-3*c* structures)	300–720 K (*I*2/*a* structure)	820–1260 K (*R*3*c* and *R*-3*c* structures)
$\alpha(a)$	10.1×10^{-6}	9.0×10^{-6}	10.0×10^{-6}	9.6×10^{-6}
$\alpha(b)$	11.0×10^{-6}	9.0×10^{-6}	12.0×10^{-6}	9.6×10^{-6}
$\alpha(c)$	8.6×10^{-6}	14.0×10^{-6}	9.0×10^{-6}	14.0×10^{-6}
α (ave)	9.9×10^{-6}	10.7×10^{-6}	10.3×10^{-6}	11.1×10^{-6}

The value of the critical temperature of LSGM-05 is in good agreement with the DSC data. The lattice constants of both RT and HT phases increase almost monotonically with temperature. Deviations will be discussed in the next paragraphs. Practically, a linear volume can be observed for the LSGM-10 in the whole temperature range investigated and discontinuity in the cell volume was detected. Deviation of the cell volume from the linear behavior is observed for the LSGM-05 sample in the temperature range 770–1020 K (Fig. 3). This deviation does not coincide with the temperature of the structural phase transition; instead it is shifted to higher temperatures by about 150 K. In order to check this observation, diffraction experiments were repeated at different experimental conditions (wavelength, beam collimation, etc.). Nevertheless, the same evolution of lattice parameters and cell volumes were obtained.

The structural transformations found in both crystals are clearly reflected by the temperature dependency of the conductivity (see below).

Taking into account the critical temperatures of the phase transitions, the average linear thermal expansion coefficients α(ave) of LSGM-05 and LSGM-10 were calculated for two temperature ranges (Table 2). The values of α(ave) are in good agreement with earlier results (for example, [8,10]). The Mcl and OR phases of both crystals show slightly smaller α(ave) values than the HT Rh phases (Table 2). Pronounced anisotropy of the thermal expansion is observed for both crystals. The anisotropy is especially noticeably in the Rh phases of both crystals, where the difference between α-values in *a*- and *c*-direction reached 45% (Table 2).

3.2. Crystal structure

For detailed studies of the RT and HT structures additionally to the RT measurements diffraction patterns of LSGM-05 at 670, 820, 1020 K and of LSGM-10 at 1260 K were collected.

3.2.1. LSGM-05 structure

Taking into account systematic absences, which indicate a body-centered lattice, the RT structure of LSGM-05 has been refined in space group *Imma*. Structure refinement using anisotropic approximation of the displacement factors for all atoms resulted in an excellent fit of experimental and calculated profiles (Fig. 4) and led to the residuals $R_I = 0.0282$, $R_P = 0.0855$. The final values of the positional parameters, as well as atomic displacement factors (adf's) are collected in Table 3; the corresponding interatomic distances are summarized in Table 4.

The LSGM-05 structure at 670 K was refined using the same model with quite satisfactory result (see Table 3). Nevertheless, a detailed examination of the diffraction profiles showed a broadening of some reflections. Broadening occurs for those reflections, which are expected to split in a Mcl cell. For the RT structure such systematic broadening has not been observed (Fig. 5). Taking into account these results, as well as the data of [6], a new refinement of both structures in Mcl symmetry (space group *I*2/*a*) was performed. Somewhat better final residuals in comparison with the OR model could be obtained for the LSGM-05 structure at 670 K, whereas no improvement of the fit or final residuals could be achieved for the RT structure (see Table 3).

Fig. 6 presents experimental and fitted data in the *d*-spacing range of 2.242–2.27 Å, corresponding to the $(202)_o$ and $(220)_o$ reflections of the OR phase, which were obtained for both, the OR and Mcl structure models. The figure shows that better fit is associated with the Mcl model for the LSGM-05 structure at 670 K, whereas for the RT structure no improvement is visible. Within experimental error, Mcl angles obtained ($\beta = 90.002(3)^\circ$) showed no deviation from the orthogonal lattice in the RT structure, whereas for the structure at 670 K a small Mcl distortion ($\beta = 90.035(2)^\circ$) was found.

In order to study the transition between the OR and Mcl structures in LSGM-05 an analysis of the HWFM values of the specified reflections in the temperature range 300–670 K has been performed (Fig. 7). Considerable broadening of the $(404)_o$ and $(211)_o$ Bragg peaks indicating the Mcl distortion begins at 570 K, whereas the HWFM values of other reflections remain practically unchanged. Hence, it may be concluded that the OR-to-Mcl phase transition of LSGM-05 occurs in the temperature range 520–570 K. The change in slope of the conductivity, which is observed in this temperature

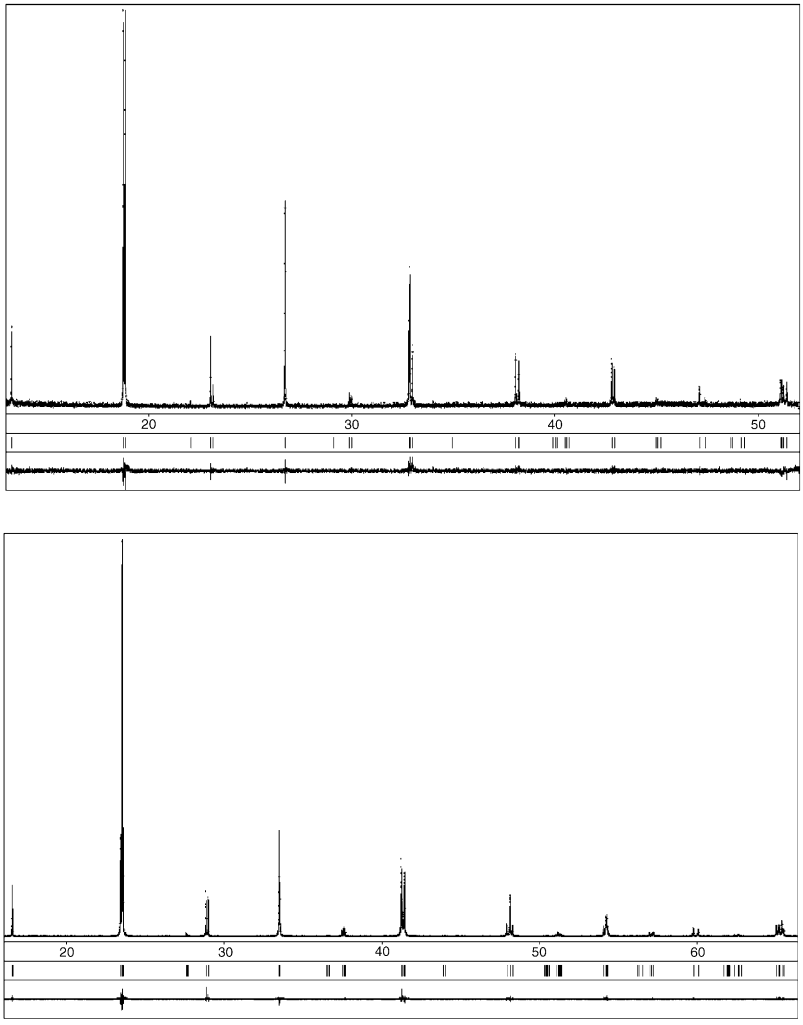

Fig. 4. Graphical results of the Rietveld refinement of the orthorhombic (RT, bottom) and rhombohedral (1020 K, top) structures of LSGM-05. Parts of the patterns covering the *d*-spacing of 3.905–1.015 Å are shown. Different values of the 2θ scale are due to the different wavelength applied ($\lambda = 1.12435$ Å for RT structure and $\lambda = 0.90812$ Å for the structure at 1020 K).

range (see below), may be associated with this transition.

As mentioned above, the peak splitting in the LSGM-05 powder patterns above 720 K clearly indicates the Rh deformation of the perovskite lattice. Our analysis of systematic absences of reflections in the patterns collected at 820 and 1020 K allows the refinement in two possible space groups: centrosymmetric *R*-3*c* and non-centrosymmetric *R*3*c*. Accordingly, both possible models were tested.

A better fit and final residuals were achieved using the acentric space group for the structure at 820 K (see Table 5). In comparison with the centrosymmetric model, this structure differs mainly in the shift of La cations. The positions of the Ga and oxygen atoms remain practically the same in both structure models.

Refinement of the structure at 1020 K in both models led to the same residuals. No improvement could be achieved in spite of more degrees of freedom in the non-centrosymmetric model. Besides, no deviation of atoms from their equivalent positions (within the limit of error) was found. Therefore, the higher symmetric *R*-3*c* space group was selected as the preferred one for LSGM-05 at 1020 K.

The transition between the non- and centrosymmetric Rh structures occurs in the temperature range 870–970 K. Probably, the above-mentioned deviation of the thermal behavior of the cell volume is associated with this transformation. Besides, the transition coincides well with the changes in the activation energy of the conductivity (see below). Tables 5 and 6 summarize the final results of the refinement of the LSGM-05 structure at 820 and 1020 K in space groups *R*3*c* and *R*-3*c*.

We conclude that LSGM-05 structure is OR (*Imma*) as RT undergoes three-phase transitions in the temperature range 300–1260 K: OR-to-Mcl at 520–570 K, Mcl-to-Rh (*R*3*c*) at 718 K, and Rh, *R*3*c*-to-Rh, *R*-3*c* at 870–970 K.

Table 3
Refined structural parameters of LSGM-05 (RT and 670 K) and LSGM-10 (RT)

Atoms	Parameters	LSGM-05, RT		LSGM-10, RT		LSGM-05, 670 K	
		Imma	*I2/a*	*Imma*	*I2/a*	*Imma* [1]	*I2/a*
	a (Å)	7.79423(3)	7.79424(3)	7.82114(6)	7.82129(5)	7.8229(2)	7.8227(2)
	b (Å)	5.49896(2)	5.53807(2)	5.51645(4)	5.54361(3)	5.5208(2)	5.5555(1)
	c (Å)	5.53806(2)	5.49892(2)	5.54352(3)	5.51654(4)	5.5555(1)	5.5208(2)
	β (deg)	90	90.002(3)	90	90.040(1)	90	90.035(2)
	V (Å^3)	237.362(2)	237.363(2)	239.175(5)	239.187(5)	239.94(2)	239.93(2)
La/Sr	x	0.25	0.25	0.25	0.25	0.25	0.25
	y	0	−0.0027(3)	0	−0.0041(3)	0	−0.003(3)
	z	−0.0032(2)	0	−0.0032(4)	0	−0.004(2)	0
	B_{eq}	1.24(2)	1.33(2)	1.18(3)	1.29(3)	2.3(2)	2.4(2)
	Site	0.95/0.05	0.95/0.05	0.90/0.10	0.90/0.10	0.95/0.05	0.95/0.05
Ga/Mg	x	0	0	0	0	0	0
	y	0	0.5	0	0.5	0	0.5
	z	0.5	0	0.5	0	0.5	0
	B_{eq}	0.92(4)	1.01(4)	0.88(6)	0.86(5)	1.7(3)	1.6(3)
	Site[a]	0.893(4)/0.107(4)	0.893(4)/0.107(4)	0.786(5)/0.214(5)	0.765(4)/0.235(4)	0.90(3)/0.10(3)	0.87(3)/0.13(3)
O1	x	0.25	0.25	0.25	0.25	0.25	0.25
	y	0	0.4325(13)	0	0.440(2)	0	0.450(12)
	z	0.4315(13)	0	0.436(2)	0	0.442(11)	0
	B_{eq}	1.7(3)	1.8(3)	1.7(4)	1.9(5)	1.7(23)	2.0(23)
	Site[a]	0.99(1)	0.97(1)	0.91(2)	0.81(2)	0.96(8)	0.96(8)
O2	x	−0.0356(7)	0.4661(9)	0.4651(11)	0.4674(14)	−0.030(10)	0.465(7)
	y	0.75	0.771(2)	0.75	0.735(4)	0.75	0.773(14)
	z	0.25	0.228(2)	0.25	0.271(3)	0.25	0.234917)
	B_{eq}	1.8(2)	1.8(2)	2.2(3)	2.1(3)	2.0(18)	2.1(18)
	Site[a]	0.900(7)	0.919(8)	0.91(1)	0.93(1)	0.86(6)	0.89(6)
	R_I	0.0282	0.0293	0.0457	0.0438	0.080	0.0773
	R_P	0.0855	0.0853	0.1473	0.1291	0.2310	0.1933

Anisotropic thermal parameters for LSGM-05 and LSGM-10 in orthorhombic and monoclinic lattices

Atoms		LSGM-05, RT		LSGM-10, RT		LSGM-05, 670 K	
		Imma	*I2/a*	*Imma*	*I2/a*	*Imma*	*I2/a*
La(Sr)	B_{11}	1.07(3)	1.09(3)	1.15(5)	1.11(4)	2.4(3)	2.8(4)
	B_{22}	1.80(3)	0.96(3)	1.28(4)	1.19(4)	2.4(3)	2.0(3)
	B_{33}	0.84(3)	1.95(4)	1.12(4)	1.57(5)	2.2(4)	2.4(4)
	B_{12}	0	0	0	0	0	0
	B_{13}	0	−0.2(2)	0	−0.28(6)	0.2940	0.2940
	B_{23}	0	0	0	0	0	0
Ga(Mg)	B_{11}	0.87(7)	0.86(7)	0.96(11)	0.93(10)	1.5(6)	0.9(6)
	B_{22}	0.95(7)	1.09(6)	0.81(10)	0.96(8)	1.8(6)	1.6(5)
	B_{33}	0.96(5)	1.07(7)	0.87(9)	0.69(10)[a]	1.7(5)	2.3(6)
	B_{12}	0	0.3(2)	0	0.1(2)	0	−0.5(13)
	B_{13}	0	−0.4(6)	−0.0(3)	0.50(14)	−0.4(13)	0.7(7)
	B_{23}	0	0.1(3)	0	−0.4(4)	0	0.9(16)
O1	B_{11}	1.3(4)	1.5(5)	0.9(6)	1.3(7)	2.3(34)	2.9(37)
	B_{22}	1.9(4)	2.1(5)	1.6(7)	2.4(9)	1.8(36)	0.9(46)
	B_{33}	1.9(5)	2.0(5)	2.6(8)	2.0(8)	0.9(49)	2.1(37)
	B_{12}	0	0	0	0	0	0
	B_{13}	0	2.1(13)	0	1.0(11)	0	1.2(53)
	B_{23}	0	0	0	0	0	0
O2	B_{11}	1.1(4)	1.9(4)	2.4(7)	2.3(6)	2.6(42)	2.9(38)
	B_{22}	2.3(3)	1.6(3)	2.4(5)	2.0(4)	2.0(24)	1.5(26)

Table 3 (*continued*)

Atoms	Parameters	LSGM-05, RT		LSGM-10, RT		LSGM-05, 670 K	
		Imma	*I2/a*	*Imma*	*I2/a*	*Imma* [1]	*I2/a*
	B_{33}	1.8(3)	1.9(4)	1.7(5)	2.0(5)	1.5(22)	1.9(26)
	B_{12}	0	−0.2(7)	0	−0.2(8)	0	−0.5(45)
	B_{13}	0	0.3(6)	0	−0.4(7)	0	0.7(38)
	B_{23}	−2.1(2)	−0.5(3)	−0.9(4)	−0.4(4)	−0.3(18)	−0.2(20)

[a] The sites occupancies were refined for fixed ratios of La/Sr (0.095/0.05, 0.90/0.10) as nominal starting compositions for the corresponding crystals.

Table 4
Selected interatomic distances (Å) and angles (deg) for the OR and Mcl models of $La_{0.95}Sr_{0.05}Ga_{0.9}Mg_{0.1}O_{3-y}$ and $La_{0.9}Sr_{0.1}Ga_{0.8}Mg_{0.2}O_{3-y}$

	Imma				*I2/a*		
	LSGM-05, RT	LSGM-10, RT	LSGM-05, 670 K		LSGM-05, RT	LSGM-10, RT	LSGM-05, 670 K
La–O1	2.407(7)	2.434(12)	2.47(7)	La–O1	2.410(8)	2.462(12)	2.52(7)
4 O2	2.559(4)	2.570(6)	2.60(4)	2O2	2.446(10)	2.474(15)	2.46(8)
2 O1	2.778(1)	2.783(2)	2.782(8)	2O2	2.698(10)	2.69(2)	2.69(8)
4 O2	2.968(4)	2.973(6)	2.94(4)	2O1	2.777(1)	2.781(2)	2.776(7)
O1	3.131(7)	3.110(12)	3.08(7)	2O2	2.849(9)	2.868(15)	2.88(7)
				2O2	3.070(10)	3.060(15)	3.08(7)
				O1	3.128(8)	3.082(12)	3.04(7)
Ga–4O2	1.9707(8)	1.974(1)	1.971(7)	Ga–2O2	1.971(12)	1.95(2)	1.96(9)
2O1	1.985(1)	1.987(2)	1.983(11)	2O2	1.981(12)	1.983(2)	1.976(9)
				2O1	1.984(1)	2.00(2)	2.01(9)
La–4Ga	3.3706(1)	3.3810(1)	3.3834(2)	La–2Ga	3.3699(1)	3.374(2)	3.3820(2)
2Ga	3.371(1)	3.377(2)	3.381(11)	2Ga	3.3700(1)	3.3806(1)	3.383(12)
2Ga	3.400(1)	3.407(2)	3.414(11)	2Ga	3.374(1)	3.3822(1)	3.3840(2)
				2Ga	3.398(1)	3.410(2)	3.411(12)
La–2La	3.877(1)	3.885(2)	3.887(14)	La–2La	3.881(1)	3.879(2)	3.892(15)
2La	3.8973(1)	3.9107(1)	3.9120(3)	2La	3.8972(1)	3.9109(1)	3.9115(2)
2La	3.927(1)	3.936(2)	3.946(14)	2La	3.924(1)	3.942(2)	3.940(15)
Ga–2Ga	3.8971(1)	3.9106(1)	3.9118(2)	Ga–2Ga	3.8971(1)	3.9106(1)	3.9114(2)
4Ga	3.9022(1)	3.9106(1)	3.9164(1)	4Ga	3.9022(1)	3.9104(1)	3.9161(1)
Ga–O1–Ga	158.0(2)	159.4(4)	161.1(21)	Ga–O1–Ga	158.3(2)	160.7(4)	163.7(22)
Ga–O2–Ga	163.8(2)	164.1(3)	166.9(20)	Ga–O2–Ga	161.8(6)	163.0(9)	161.9(44)

3.2.2. *LSGM-10 structure*

The RT structure of LSGM-10 was analyzed using two possible structure models (*Imma* and *I2/a*). In contrast to LSGM-05, the structure refinement in the Mcl model showed a better fit between experimental and calculated profiles (Fig. 6) and led to the final residuals $R_I = 0.0438$, $R_P = 0.1291$. The Mcl distortion of the LSGM-10 structure is confirmed by the diffraction profiles of the pattern, especially the broadening of the peaks, which split in the case of the Mcl lattice (Fig. 5). The graphical results of the Rietveld refinement of the RT LSGM-10 structure in *I2/a* space group are plotted in Fig. 8. The final atomic parameters, as well as adf's are given in Table 3, and the corresponding interatomic distances are shown in Table 4. For comparison, the results of the structure refinement in the OR symmetry are presented as well.

Our results are in agreement with the data of Slater et al. [6], who reported Mcl symmetry for LSGM-10 up to 770 K. Because of the relatively small distortion from OR symmetry for RT and 520 K the authors named these structure as Mcl (pseudo-OR), whereas the structure at 770 K was considered Mcl (pseudo-Rh). As mentioned above, we found the structure at 770 K to be of two coexisting phases.

The powder diffraction pattern of LSGM-10, collected at 1260 K, was refined in Rh symmetry in two possible space groups: *R*3*c* and *R*-3*c*. Tables 6 and 7 summarize the final atomic parameters and interatomic distances for both models.

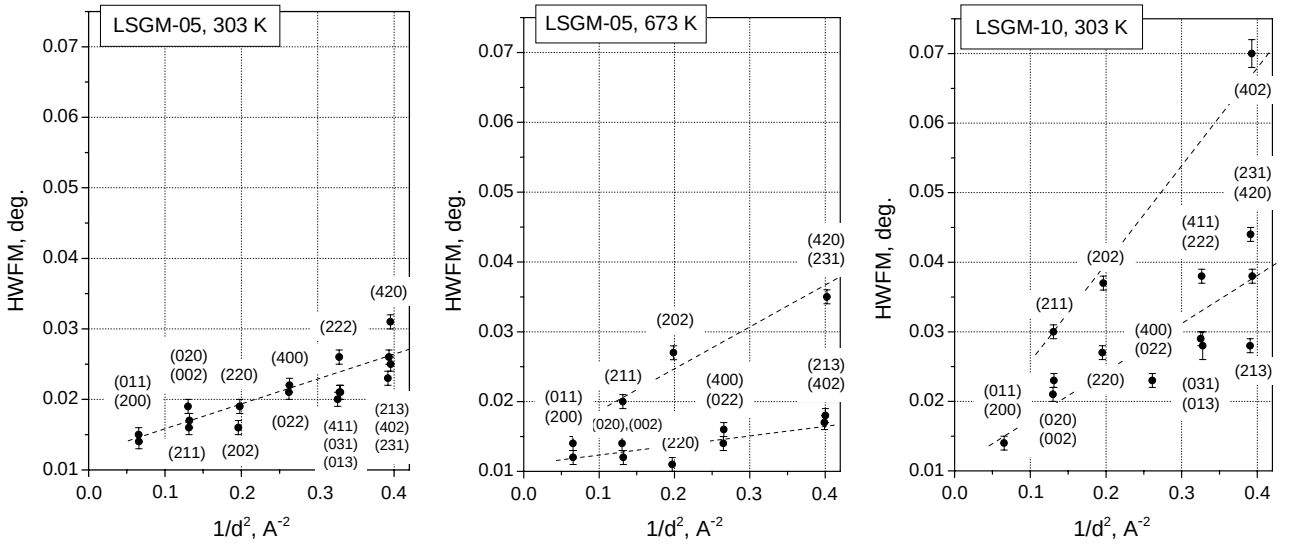

Fig. 5. HWFM values of LSGM reflections. Systematic broadening of the $(211)_o$, $(202)_o$ and $(402)_o$ orthorhombic reflections associated with the monoclinic deformation of LSGM-05 (670 K) and LSGM-10 (RT).

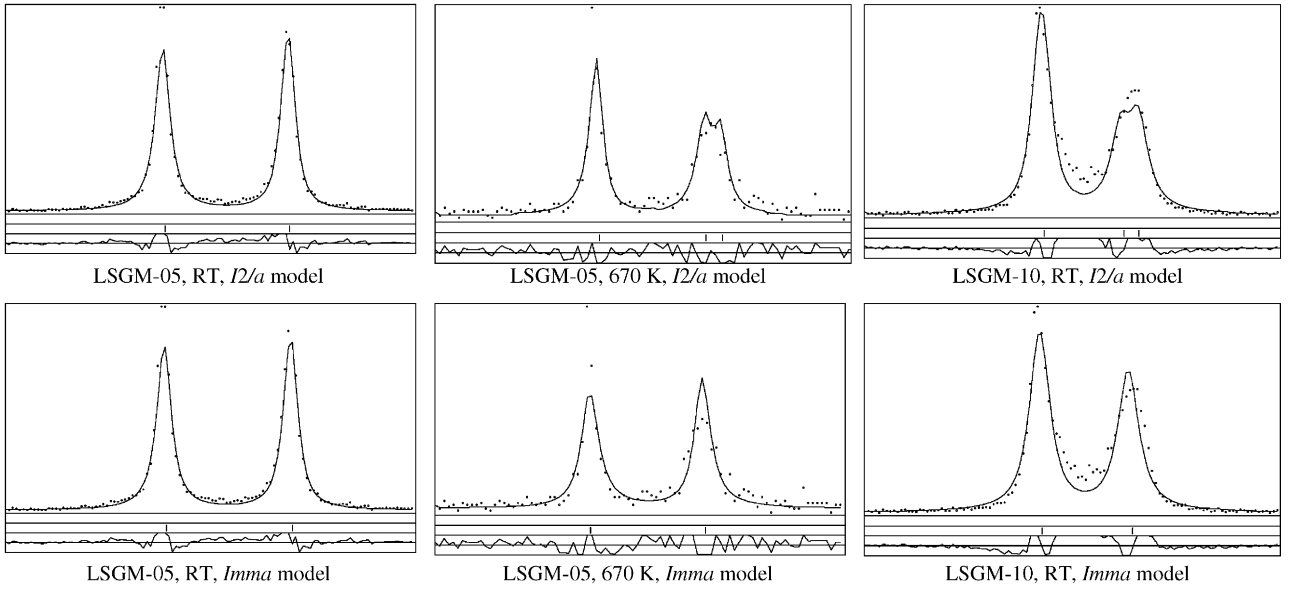

Fig. 6. Examples of profile fitting of $(220)_o$ and $(202)_o$ reflections for LSGM-05 and LSGM-10 using different structure models and symmetries.

In contrast to the results of Slater who described the 1270 K structure in *R*3*c* space group [6], we did not find indications for an acentric lattice. In spite of the increased number of parameters, the refinement in the non-centrosymmetric space group did not lead to an improved fit; instead it showed even somewhat worse residuals. These facts as well as detailed comparative analysis of both structure models show that the high-symmetry phase in *R*-3*c* space group is preferable for the HT structure of LSGM-10. Possibly two different Rh phases exist in this structure above 770 K, similar as in LSGM-05. A second phase transition from the Mcl (pseudo-Rh) to the Rh structure occurred in the temperature range 770–1020 K (as reported in [6]). This is in fact the transition between two different Rh structures. Another confirmation of this assumption is the change of the activation energy of the conductivity, which is observed in Arrhenius plots of the corresponding curves (Chapters 3 and 4).

3.3. Site occupancies and oxygen diffusion pass

Refinements of the Ga/Mg and oxygen site occupancies performed at fixed La/Sr ratio are in good agreement with the nominal starting composition for both crystals (see Table 3). Repeated refinements of the

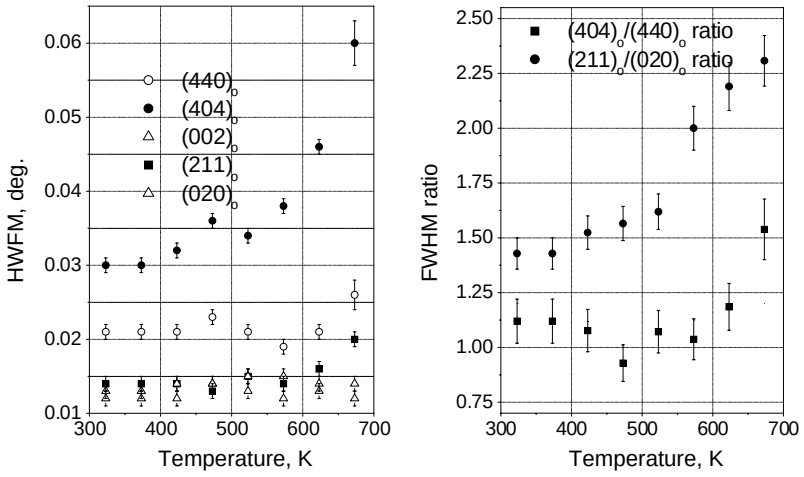

Fig. 7. Thermal evolution of the HWFM values of $(440)_o$, $(404)_o$, $(211)_o$, $(020)_o$ and $(002)_o$ reflections (left) and their ratio (right) for the LSGM-05 structure.

Table 5
Refined structural parameters of the rhombohedral structures of LSGM-05 and LSGM-10 crystals

		LSGM-05, 820 K		LSGM-05, 1020 K		LSGM-10, 1260 K	
		R-3*c*	*R*3*c*	*R*-3*c*	*R*3*c*	*R*-3*c*	*R*3*c*
	a (Å)	5.55622(8)	5.55628(8)	5.56689(6)	5.56687(5)	5.5894(1)	5.58985(8)
	c (Å)	13.5086(3)	13.5088(3)	13.5528(2)	13.5528(2)	13.6644(4)	13.6654(3)
	V (Å^3)	361.16(2)	361.17(2)	363.73(1)	363.73(1)	369.79(2)	369.79(2)
La/Sr	*x*	0	0	0	0	0	0
	y	0	0	0	0	0	0
	z	0.25	0.2604(8)	0.25	0.2541(12)	0.25	0.257(6)
	B_{eq}	1.5(2)	2.72(14)	2.3(2)	2.45(8)	2.0(12)	2.0(5)
	B_{11}, B_{22}	0.9(3)	1.5(2)	2.2(2)	2.27(9)	1.9(13)	1.9(6)
	B_{33}	2.9(4)	5.2(3)	2.6(3)	2.6(2)	2.2(24)	2.2(11)
	B_{12}	$1/2B_{11}$	$1/2B_{11}$	$1/2B_{11}$	$1/2B_{11}$	$1/2B_{11}$	$1/2B_{11}$
	B_{13}, B_{23}	0	0	0	0	0	0
	Site	0.95/0.05	0.95/0.05	0.95/0.05	0.95/0.05	0.95/0.05	0.95/0.05
Ga/Mg	*x*	0	0	0	0	0	0
	y	0	0	0	0	0	0
	z	0	−0.0010(10)	0	0.0006(14)	0	0.007(5)
	B_{eq}	1.5(5)	1.5(2)	1.8(2)	1.82(13)	2.5(16)	1.9(8)
	B_{11}, B_{22}	0.3(5)	1.7(3)	1.9(3)	1.99(15)	2.8(18)	2.4(9)
	B_{33}	3.8(9)	0.9(4)	1.7(5)	1.5(2)	1.8(32)	1.0(15)
	B_{12}	$1/2B_{11}$	$1/2B_{11}$	$1/2B_{11}$	$1/2B_{11}$	$1/2B_{11}$	$1/2B_{11}$
	B_{13}, B_{23}	0	0	0	0	0	0
	Site[a]	0.87(6)/0.13(6)	0.90(3)/0.10(3)	0.91(3)/0.09(3)	0.90(1)/0.10(1)	0.81(2)/0.09(2)	0.80(2)/0.20(2)
O	*x*	0.463(11)	0.462(4)	0.453(7)	0.453(3)	0.461(9)	0.451(9)
	y	0	0.006(5)	0	0.004(6)	0	−0.003(16)
	z	0.25	0.252(3)	0.25	0.246(4)	0.25	0.243(7)
	B_{eq}	5.0(22)	5.2(15)	5.3(16)	4.1(26)	7.6(64)	4.7(34)
	B_{11}			6.0(21)	2.2(38)	9.5(83)	6.7(34)
	B_{22}			4.4(20)	4.1(10)	4.5(87)	3.8(46)
	B_{33}			4.8(23)	3.6(11)	7.2(93)	3.2(55)
	B_{12}			$1/2B_{22}$	−0.3(41)	$1/2B_{22}$	2.3(30)
	B_{13}			−2.1(8)	−0.9(38)	−1.2(34)	0.7(**)
	B_{23}			$2B_{13}$	−1.1(8)	$2B_{13}$	0.1(32)
	Site[a]	0.98(6)	0.97(3)	0.95(5)	0.95(2)	0.94(4)	0.93(4)
	R_I	0.0593	0.0581	0.0522	0.0522	0.0294	0.0314
	R_P	0.2008	0.1957	0.1466	0.1478	0.1522	0.1579

[a] The sites occupancies were refined at the fixed La/Sr (0.095/0.05, 0.9/0.1) nominal starting composition for the corresponding crystals.

Table 6
Selected interatomic distances (Å) and angles (deg) of the rhombohedral structures of $La_{0.95}Sr_{0.05}Ga_{0.9}Mg_{0.1}O_{3-y}$ and $La_{0.9}Sr_{0.1}Ga_{0.8}Mg_{0.2}O_{3-y}$

R-3*c*				*R*3*c*			
Distances	LSGM-05, 820 K	LSGM-05, 1020 K	LSGM-10, 1260 K	Distances	LSGM-05, 820 K	LSGM-05, 1020 K	LSGM-10, 1260 K
La–3O	2.57(6)	2.52(4)	2.58(17)	La–3O	2.55(3)	2.51(3)	2.54(10)
6O	2.772(4)	2.784(4)	2.800(14)	3O	2.66(3)	2.68(5)	2.67(23)
3O	2.98(6)	3.05(4)	3.01(17)	3O	2.89(3)	2.89(5)	2.95(24)
				3O	3.01(3)	3.06(3)	3.07(10)
Ga–6O	1.970(6)	1.982(5)	1.99(2)	Ga–3O	1.93(3)	1.96(4)	1.87(14)
				3O	2.02(3)	2.01(4)	2.12(15)
La–2Ga	3.3771(3)	3.3882(2)	3.4166(7)	La–Ga	3.22(2)	3.34(3)	3.41(30)
6Ga	3.3997(1)	3.4067(1)	3.4225(3)	3Ga	3.352(5)	3.391(8)	3.42(10)
				3Ga	3.453(6)	3.423(9)	3.43(10)
				Ga	3.53(2)	3.44(3)	3.43(30)
La–6La	3.9191(2)	3.9284(1)	3.9503(5)	La–6La	3.919(9)	3.928(14)	3.95(20)
Ga–6Ga	3.9191(2)	3.9284(1)	3.9503(5)	Ga–6Ga	3.919(11)	3.93(2)	3.95(13)
O–4O	2.77(3)	2.78(2)	2.80(8)	O–2O	2.76(4)	2.78(6)	2.80(18)
4O	2.80(2)	2.820(13)	2.82(7)	2O	2.77(5)	2.79(3)	2.80(13)
				2O	2.78(5)	2.79(6)	2.81(18)
				2O	2.86(4)	2.86(3)	2.86(13)
Ga–O–Ga	168.2(20)	164.8(13)	167.3(57)	Ga–O–Ga	166.7(18)	163.6(21)	162.3(76)

site occupancy starting from different structural models and using various refinement strategies always led to the same results of different distributions of oxygen vacancies in LSGM-05 and LSGM-10 crystals. In LSGM-05 at RT and 670 K oxygen vacancies are located mainly in the equatorial oxygen positions (eight-fold O2 site), whereas vertexes of GaO_6 octahedra remain practically fully occupied (Fig. 9a). This distribution is observed independently of the structure models applied (OR or Mcl). In contrast to LSGM-05, the oxygen vacancies in the LGSM-10 structure are located mainly on the O1 sites (apical O-positions in vertexes of the GaO_6 octahedron) (Fig. 9b). Slater et al. [6] reported similar oxygen vacancies in the monoclinic LSGM-10 structure. Accordingly in the LSGM-05 structure two kinds of jumps are possible: O1→2 and O2→2 (Fig. 9a), whereas in LSGM-10 only O2→1 jumps are expected (Fig. 9b). (The notations 2 and 1 indicate the oxygen vacancies in O2 and O1 positions, respectively.) Our structural refinements are supported by differing behavior of the conductivity of both crystals.

In contrast to the OR and monoclinic phases only one equivalent oxygen site in the Rh structure exists. Hence, in both HT structures above 820 K the precise position of the vacancy in the BO_6 polyhedron cannot be determined.

In their MD calculations authors [21,22] showed for the cubic and OR structural models of LSGM-10 that lattice relaxation effects allow for oxygen diffusion. Our detail structural refinement showed that the symmetry of LSGM-05 and LSGM-10 at HT is in fact Rh. Considering this deformation state and relaxation effects we propose the following mechanism.

To move from its regular position to a vacancy site, the migrating oxygen ion passes through a triangle, formed by one Ga^{3+} and two La^{3+} cations (Fig. 9). Four kinds of La–Ga–La triangles with different areas exist in the OR structure, whereas in the Mcl structure six different triangles are formed. Three, respectively two kinds of triangles exist in the Rh *R*3*c* and *R*-3*c* structures (Table 7). In most of the structures, the differences between the areas of different triangles are in the limit of 1–2%; however, in the case of rhombohedral LSGM-05 at 820 K it is 9%. From the interatomic distances (Tables 4 and 6) and the radii of corresponding cations [23] the estimated radii of the inscribed circles are 1.1–1.2 Å. Taking into account the O^{2-} anion radius (1.4 Å, after Shannon [23]), the structure cannot simply be considered as a hard-sphere lattice with fixed ions as authors [21,22] previously pointed out. Transport of the O^{2-} ions through the triangles must be accompanied by shifts (relaxation) of cations and/or deformations (polarization) of O^{2-} ions. The pathway of the O^{2-} ions along the edge of octahedra cannot be linear. The route is along an arc curved away from the Ga atom (Fig. 9a and b). The maximum deviation from linearity calculated from the atomic coordinates and ionic radii is 0.1–0.13 Å, even if calculations are purely based on geometrical considerations, assuming the cations as

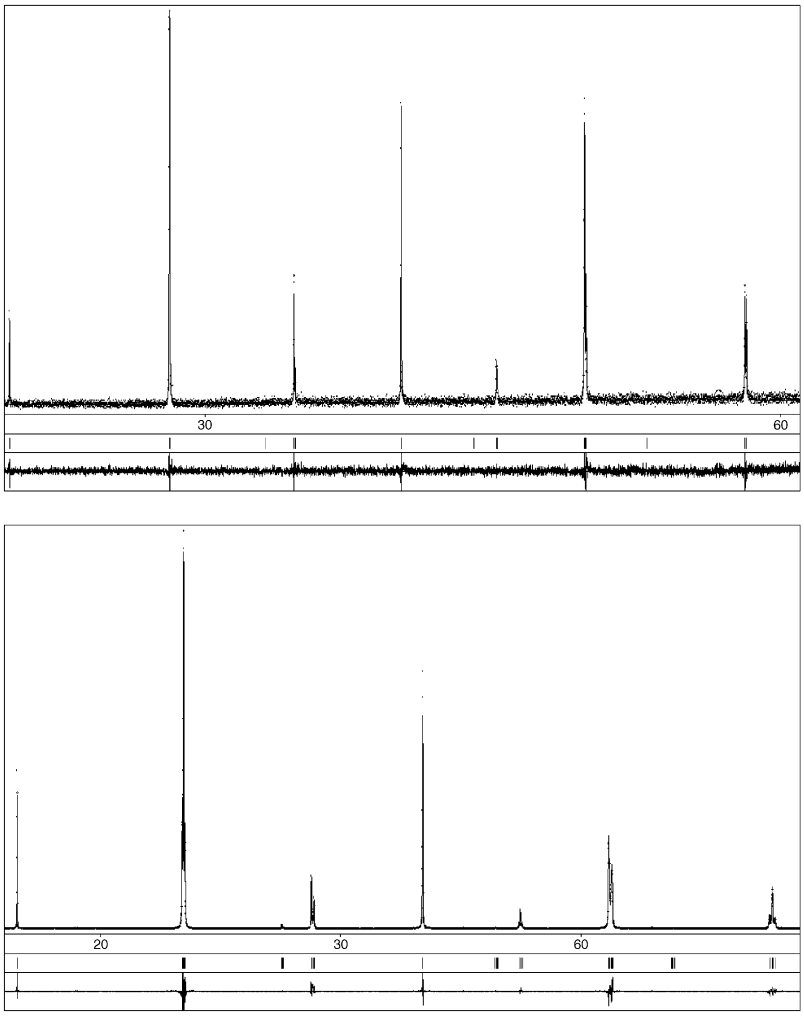

Fig. 8. Plot of the Rietveld refinement of the monoclinic (RT, bottom) and rhombohedral (1260 K, top) structures of LSGM-10. Parts of the patterns covering the *d*-spacing of 3.910–1.322 Å are shown. Different 2θ scales are due to the different wavelength applied ($\lambda = 1.12435$ Å for RT structure and $\lambda = 1.35711$ Å for the structure at 1260 K).

Table 7
Areas of the triangles (Å^2) built by two La^{3+} and one Ga^{3+} ions in the LSGM-05 and LSGM-10 structures

Triangle	LSGM-05				LSGM-10	
	RT *Imma*	670 K *I*2/*a*	820 K *R*3*c*	1020 K *R*-3*c*	RT *I*2/*a*	1260 K *R*-3*c*
S1	5.323 × 2	5.386	5.170 × 2	5.445 × 4	5.361	5.512 × 4
S2	5.345 × 2	5.388	5.450 × 4	5.468 × 4	5.363	5.519 × 4
S3	5.358 × 2	5.398 × 2	5.664 × 2		5.393 × 2	
S4	5.414 × 2	5.433 × 2			5.421 × 2	
S5		5.450			5.450	
S6		5.453			5.453	
S average	5.36	5.417	5.435	5.456	5.405	5.516

fixed spheres. Other authors [21,23] performed molecular dynamic simulations of oxygen diffusion and predicted also small deviations from a linear pathway. The authors found significant outward relaxation (~0.1 Å) of the triangle forming cations, away from the mobile oxygen ion, which probably reduces repulsive overlap interactions. Lerch and Boysen [7] also concluded from there analysis of probability density function (pdf) maps that diffusion of the anions occurs near an arc of a circle above the edges of the octahedra.

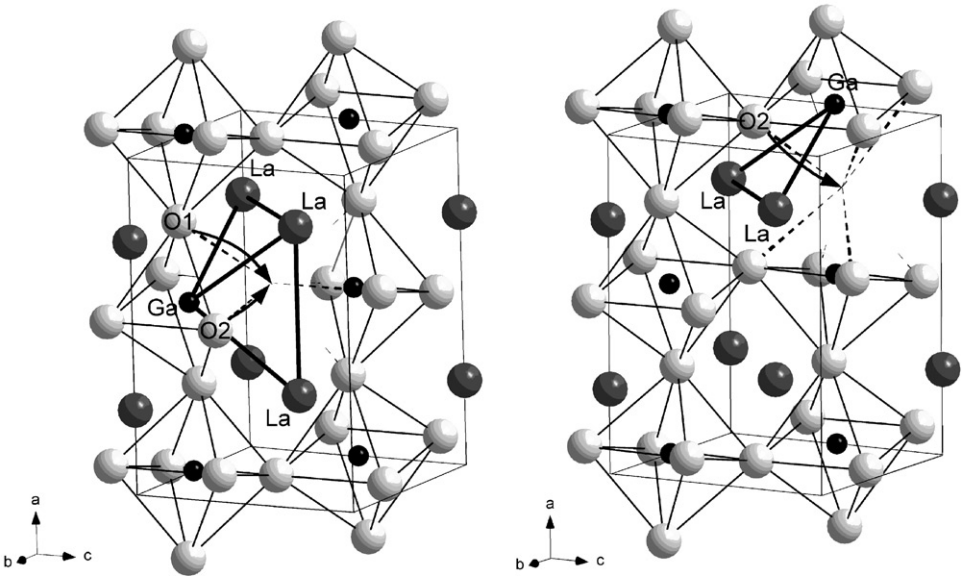

Fig. 9. Projection of the LSGM-05 (left) and LSGM-10 (right) structure showing different locations of oxygen vacancies and possible pathways of anion migration.

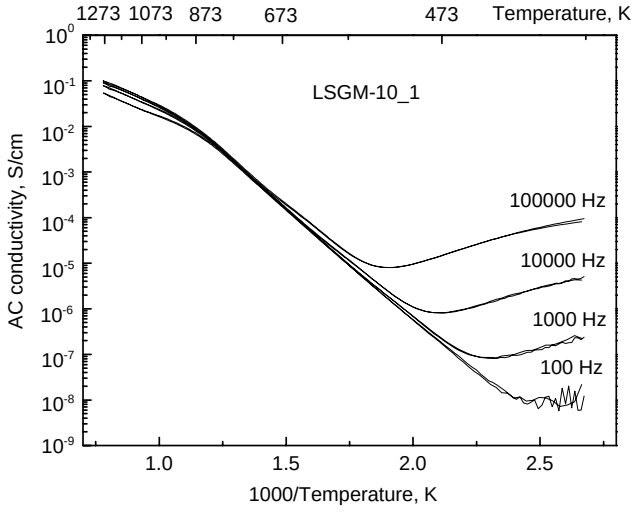

Fig. 10. Temperature dependence of the real part of the AC conductivity of crystal sample LSGM-10_1 measured at different frequencies.

Different oxygen vacancy distributions in LSGM-05 and LSGM-10, as well as their structural characteristics seem to explain the different conductivity in both crystals.

3.4. Conductivity

Fig. 10 illustrates the thermal evolution of the conductivity (σ) of the crystal sample LSGM-10_1 (Table 8) measured at different frequencies. The conductivity values in the high-temperature region approach the same value at all frequencies. The frequency of 1000 Hz was chosen as a reference for further conductivity studies in this work. The conductivity was measured in the temperature range 570–1270 K. The small imaging part of the resistance could be neglected for all samples.

Figs. 11 and 12 display the behavior of the conductivity versus temperature during heating/cooling of the LSGM-05 and LSGM-10 samples, respectively. The conductivity values collected on heating resemble the data on cooling. Three temperature intervals with different activation energies are seen in Table 8 for LSGM-05 and LSGM-10 between 570 and 1270 K.

Generally the activation energy decreases at higher temperatures if cubic symmetry is approached. The studied samples remain Rh and anisotropic at high temperatures and, hence, the activation energy does not follow the classical trend. Changes of the slope of the conductivity curves coincide with the structural transitions and thermal expansion anomalies (see Sections 3.1 and 3.2).

In Fig. 11, an increase of the slope of the conductivity versus temperature for LSGM-05_1 and LSGM-05_2 is displayed. The change in slope above 570 K is related to the transition of the crystals from the orthorhombic RT modification to the Mcl phase. Further heating of LSGM-05 is accompanied by anomaly in the conductivity near 710 K, which is consistent with the observed discontinuities of the thermal expansion (Fig. 3) and with the transition of the Mcl to the Rh ($R3c$) phase. Surprisingly, the minimum of the activation energy is observed in the temperature range 720–970 K (Table 8), which corresponds to the acentric Rh structure of LSGM-05. Probably, the reason of such behavior in R3c phase is the La–Ga–La triangles with maximum

Table 8
Crystal structure and conductivity parameters of LSGM-05_n and LSGM-10_n crystal samples

Sample abbreviation	Crystal surface orientation (%)					Temperature range (K)	Activation energy (eV)
	$(001)_o$ $\{110\}_p$	$(211)_o$	$(010)_o$	$(100)_o$ $\{100\}_p$	$(011)_o$		
LSGM-05_01	0	0	0	55	45	970–1270 720–970 570–720	1.150 0.631 0.843–0.246
LSGM-05_02	0	0	0	70	30	970–1270 720–970 570–720	1.145 0.631 0.843–0.40
LSGM-05_05	5	75	20	0	0	970–1270 720–970 570–720	1.085 0.540 0.843
LSGM-05_06	10	50	40	0	0	970–1270 720–970 570–720	1.062 0.537 0.843
LSGM-05_07	20	5	75	0	0	970–1270 720–970 570–720	1.140 0.538 0.843
LSGM-10_01	0	0	0	100[a]		1270–870 870–570	0.541 1.077
LSGM-10_02	0	0	0	100[a]		1270–1120 1120–870 870–570	1.029 0.541 1.01
LSGM-10_03	0	0	0	100[a]		1000–850 1120–870 870–570	1.029 0.541 1.01
LSGM-10_05	20	70	10	0	0	1000–850 1120–870 870–570	1.029 0.541 1.01
LSGM-10_06	13	79	8	0	0	1000–850 1120–870 870–570	1.029 0.541 1.01

[a] Due to the equality of the $d_{(200)}$ and $d_{(001)}$ interplanar distances in LSGM-10 the reflections from the corresponding planes could not be separated.

areas of 5.664 Å^2 (Table 7). For all LSGM-05 samples an additional increase of the activation energy occurs near 870–970 K. This is in accordance with the transition of the crystals from the acentric (*R*3*c*) to the centrosymmetric (*R*-3*c*) Rh phases.

Phase transformations are reflected differently in the conductivity along different crystallographic directions. The *Imma*–*I*2/*a* transition is clearly visible in the conductivity of the samples oriented parallel to $(100)_o$ and $(011)_o$ planes (LSGM-05_1 and LSGM-05_2 specimens). In contrast, the *I*2/*a*–*R*3c transformation is better seen in conductivity of the {211}-oriented plates (samples LSGM-05_5,6,7).

Similar relations between conductivity and structural characteristics can be observed for LSGM-10 samples. The decreasing activation energy near 770 K on heating is correlated with the transition of the crystals from the Mcl to the high-temperature Rh phase. The increase of the activation energy in the temperature range 920–1020 K corresponds to the transition from the rhombohedral *R*3*c* to the *R*-3*c* phase.

The conductivities of LSGM-05 and LSGM-10 in the high-temperature region tend to approach equal values independent from crystal orientation which indicates an increase of the crystal symmetry with temperature. The difference in size between different La–Ga–La triangles

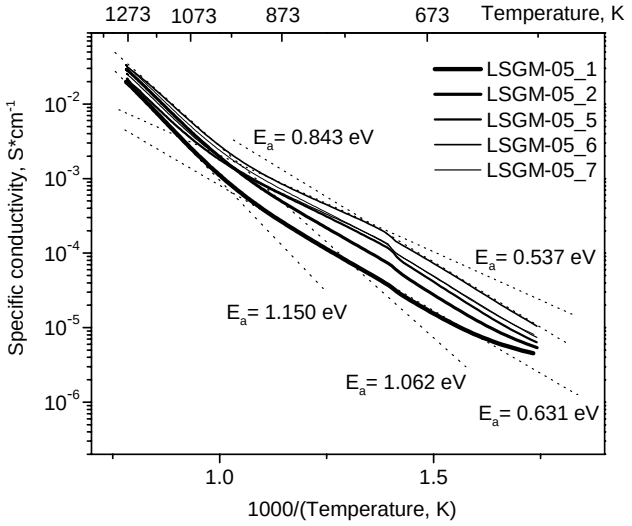

Fig. 11. Temperature behavior of the AC conductivity of crystal samples LSGM-05_n measured at 1000 Hz in air.

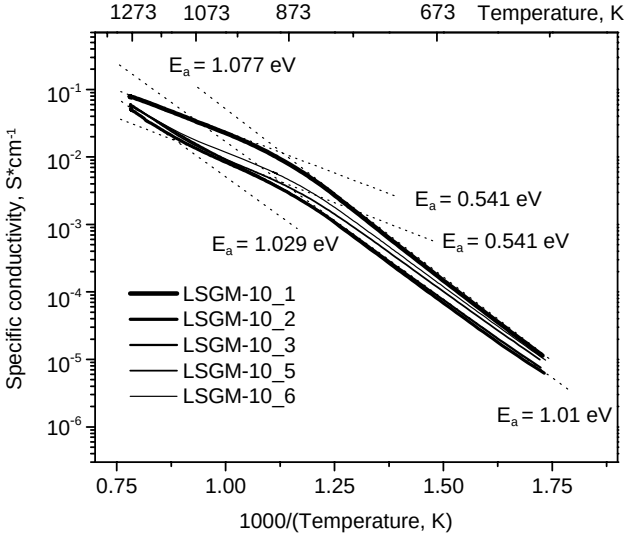

Fig. 12. Temperature dependence of the AC conductivity of crystal samples LSGM-10_n measured at 1000 Hz in air.

in the HT *R*-3*c* phases (Table 7) does not exceed 0.1–0.4%. Therefore, the transport of oxygen ions in different directions occurs with nearly equal probability.

The conductivity of the LSGM-10 (Fig. 12) is somewhat higher in comparison with that of LSGM-05 (Fig. 11). This may be explained by an increasing concentration of oxygen vacancies after the substitution of La^{3+} by Sr^{2+} and Ga^{3+} by Mg^{2+} according to the following defect reactions written in Kröger-Vink notation:

$$2SrO + 2La_{La}^{x} + O_{O}^{x} = 2Sr'_{La} + V_{O}^{\bullet\bullet} + La_2O_3,$$

$$2MgO + 2Ga_{Ga}^{x} + O_{O}^{x} = 2Mg'_{Ga} + V_{O}^{\bullet\bullet} + Ga_2O_3.$$

The authors [21,22] suggested the formation of clusters of defects in LSGM-10. Interactions between dopant ions (Sr'_{La}) or (Mg'_{Ga}) and oxygen vacancies ($V_{O}^{\bullet\bullet}$) may lead to such formation of clusters ($Sr'_{La} - V_{O}^{\bullet\bullet}$) or ($Mg'_{Ga} - V_{O}^{\bullet\bullet}$), which can trap migrating oxygen ions (vacancies). The highest cluster binding energy in the series of possible clusters by doping of $LaGaO_3$ with SrO, CaO or MgO was calculated for ($Mg'_{Ga} - V_{O}^{\bullet\bullet}$) to be 1.37 eV [21]. For $La_{1-x}Sr_xGa_{1-x}Mg_yO_{3-\delta}$ this high binding cluster energy determined by Huang and Petric [11] and Huang et al. [24] was accepted as the reason for an increase of the experimentally determined activation energy of conduction. The observed absolute change of the conduction activation energy for LSGM-05 and LSGM-10 can be explained by the predominance of different clusters ($Mg'_{Ga} - V_{O}^{\bullet\bullet}$) or ($Sr'_{La} - V_{O}^{\bullet\bullet}$) at the same thermal conditions.

In Figs. 11 and 12 the single-crystal conductivity of the two LSGM samples is shown. The conductivity at 1 kHz behaves similar to the conductivity at higher frequencies and hence, the thermal evolution of σ for 1 kHz is displayed indicating the bulk behavior of the samples. However, to make a final decision about the character of the conductivity additional investigation is needed, in particular in different $p(O_2)$ atmospheres.

4. Conclusions

Studies of the crystal structures of $La_{1-x}Sr_xGa_{1-2x}Mg_{2x}O_{3-y}$ ($x = 0.05$, 0.1) using high-resolution powder diffraction synchrotron radiation techniques demonstrate that the RT symmetry of the crystal with $x = 0.05$ is OR (*Imma*, $a = 7.79423(3)$ Å, $b = 5.49896(2)$ Å, $c = 5.53806(2)$ Å), whereas the symmetry of the $x = 0.1$ crystal is Mcl (*I*2/*a*, $a = 7.82129(5)$ Å, $b = 5.54361(3)$ Å, $c = 5.51654(4)$ Å, $\beta = 90.040(1)^\circ$).

$La_{0.95}Sr_{0.05}Ga_{0.9}Mg_{0.1}O_{2.92}$ undergoes three phase transitions: OR-to-Mcl (*Imma*–*I*2/*a*) at 520−570 K, monoclinic-to-rhombohedral (*I*2/*a*–*R*3*c*) at 720 K and rhombohedral-to-rhombohedral (*R*3*c*–*R*-3*c*) at ca. 870 K. In $La_{0.9}Sr_{0.1}Ga_{0.8}Mg_{0.2}O_{2.85}$ a monoclinic-to-rhombohedral (*I*2/*a*–*R*3*c*) transition is observed at 770 K. Conductivity measurements indicate a second-phase transition in this crystal (*R*3*c*–*R*-3*c*) at 870–970 K.

Different distribution of oxygen vacancies has been found in both crystals. In LSGM-05 below 720 K the oxygen vacancies are basically located in the equatorial oxygen positions, whereas the vertexes of GaO_6 octahedra remain practically fully occupied. In contrast, oxygen vacancies in the LGSM-10 structure are located mainly in the apical O-positions in vertexes of the GaO_6 octahedra.

The behavior of the AC conductivity of $La_{1-x}Sr_xGa_{1-2x}Mg_{2x}O_{3-y}$ single crystals is compatible

with the anisotropy of the thermal expansion and with the thermal evolution of its structure.

Acknowledgments

The work was supported by WTZ (UKR-01/12), Deutsche Forschungs Gesellschaft (Project GU-484/1-3), Polish Committee for Scientific Research (Grant N 7 T08A 00520) and ICDD Grant-in-aid program. The authors thank to Dr. N. Tamura (Lawrence Berkeley National Laboratory, Advanced Light Source) for the Lauer experiments with micro-beams. L.Vasylechko acknowledges the Max-Planck-Society for a research fellowship.

References

[1] T. Ishihara, H. Matsuda, Y. Takita, J. Am. Chem. Soc. 116 (1994) 3801–3803.
[2] M. Feng, J.B. Goodenough, Eur. J. Solid State Inorg. Chem. 31 (1994) 663–672.
[3] T. Ishihara, H. Matsuda, Y. Takita, Solid State Ionics 79 (1995) 147–151.
[4] J. Drennan, V. Zelisko, D. Hay, F.T. Ciacchi, S. Rajendran, S.P.S. Badwal, J. Mater. Chem. 7 (1) (1997) 79–83.
[5] P.R. Slater, J.T.S. Irvine, T. Ishihara, Y. Takita, Solid State Ionics 107 (1998) 319–323.
[6] P.R. Slater, J.T.S. Irvine, T. Ishihara, Y. Takita, J. Solid State Chem. 139 (1998) 135–143.
[7] M. Lerch, H. Boysen, T. Hansen, J. Phys. Chem. Solids 62 (2001) 445–455.
[8] T. Ishihara, M. Honda, T. Shibayama, H. Minami, H. Nishiguchi, Yu. Takita, J. Electrochem. Soc. 145 (9) (1998) 3177–3183.
[9] J.W. Stewenson, T.R. Armstrong, D.E. McGready, L.R. Pederson, W.J. Weber, J. Electrochem. Soc. 144 (1997) 3613–3619.
[10] H. Hayashi, M. Suzuki, H. Inaba, Solid State Ionics 128 (2000) 131–139.
[11] P. Huang, A. Petric, J. Electrochem. Soc. 143 (1996) 1644–1647.
[12] N. Trofimenko, H. Ullmann, Solid State Ionics 118 (1999) 215–227.
[13] V.V. Kharton, A.P. Viskup, A.A. Yaremchenko, et al., Solid State Ionics 132 (2000) 119–130.
[14] I.K. Bdikin, I.M. Shmytko, A.M. Balbashov, J. Appl. Crystallogr. 26 (1993) 71–76.
[15] S.B. Ubizskii, L.O. Vasylechko, D.I. Savytskii, A.O. Matkovskii, I.M. Syvorotka, Supercond. Sci. Technol. 7 (1994) 766–772.
[16] R. Uecker, P. Reiche, V. Alex, J. Doerschel, R. Schalge, J. Cryst. Growth 137 (1994) 278–282.
[17] L. Vasylechko, D. Savytskii, A. Senyshyn, C. Bähtz, M. Knapp, U. Bismayer, M. Berkowski, A. Matkovskii, HASYLAB Annu. Rep. 1 (2001) 549–550.
[18] L.G. Akselrud, P.Yu. Zavalij, Yu. Grin, V.K. Pecharsky, B. Baumgartner, E. Woelfel, Mater. Sci. Forum 133–136 (1993) 335–340.
[19] L. Vasylechko, R. Niewa, H. Borrmann, M. Knapp, D. Savytskii, A. Matkovski, U. Bismayer, M. Berkowski, Solid State Ionics 143 (2001) 219–227.
[20] L. Vasylechko, D. Savytski, A. Matkovski, M. Berkowski, M. Knapp, U. Bismayer, J. Alloys Compds. 328 (1–2) (2001) 264–271.
[21] M.S. Islam, J. Mater. Chem. 10 (2000) 1027–1038.
[22] M.S. Khan, M.S. Islam, D.R. Bates, J. Phys. Chem. B 102 (1998) 3099–3104.
[23] R.D. Shannon, Acta Crystallogr. A 32 (1976) 751–767.
[24] P. Huang, R.S. Tichy, J.B. Goodenough, J. Am. Ceram. Soc. 81 (1998) 2565–2575.